Finite Element Implementation of Maxwell's Equations for Image Reconstruction in Electrical Impedance Tomography

Nirmal K. Soni*, *Member, IEEE*, Keith D. Paulsen, *Member, IEEE*, Hamid Dehghani, and Alex Hartov, *Member, IEEE*

***Abstract*—Traditionally, image reconstruction in electrical impedance tomography (EIT) has been based on Laplace's equation. However, at high frequencies the coupling between electric and magnetic fields requires solution of the full Maxwell equations. In this paper, a formulation is presented in terms of the Maxwell equations expressed in scalar and vector potentials. The approach leads to boundary conditions that naturally align with the quantities measured by EIT instrumentation. A two-dimensional implementation for image reconstruction from EIT data is realized. The effect of frequency on the field distribution is illustrated using the high-frequency model and is compared with Laplace solutions. Numerical simulations and experimental results are also presented to illustrate image reconstruction over a range of frequencies using the new implementation. The results show that scalar/vector potential reconstruction produces images which are essentially indistinguishable from a Laplace algorithm for frequencies below 1 MHz but superior at frequencies reaching 10 MHz.**

***Index Terms*—(A, Φ) formulation, electrical impedance tomography, finite element method, high-frequency EIT, inverse problems, Maxwell's equations.**

I. Introduction

ELECTRICAL impedance tomography (EIT) is an imaging modality wherein the spatial map of conductivity and permittivity inside a medium is obtained from a set of surface electrical measurements [1]–[3]. Electrodes are brought into contact with the surface of the object being imaged and a set of voltages (or currents) are applied and the corresponding currents (or voltages) are measured. These voltages and currents are then used to estimate the electrical properties of the object often using an image reconstruction algorithm which relies on an accurate model of the electrical interaction. The process of property estimation is highly nonlinear, ill-conditioned, and ill-posed [4].

Although EIT systems at Dartmouth operate in both voltage drive (applying voltages and measuring currents) and current drive (applying currents and measuring voltages) modes, we favor the acquisition of data primarily in voltage drive mode for several reasons: in our hands image reconstruction is less sensitive to the initial property estimate and is more tolerant to measurement noise in voltage mode relative to current mode [5], the type I (Dirichlet) boundary conditions on the electrodes are numerically stronger than their type II (Neumann) counterparts, and the instrumentation associated with precise broad-band current sources is fairly difficult to realize in hardware. In practice, effective current drive can be achieved through voltage source adjustments as in [6] and it is possible to reverse the role of the data in the reconstruction independently of how it was collected when both voltage and current are measured [7].

The interaction of electromagnetic fields with the object being imaged is governed by Maxwell's equations. Traditionally, low frequency signals are used such that a static field assumption is valid which simplifies the mathematics to Laplace's equation. At higher frequencies, however, the model must be modified because the electric and magnetic fields are increasingly coupled, and both contribute to the current and voltage distribution [8], [9].

Multispectral imaging with applied electrical currents is motivated by the fact that biological tissues have been shown to exhibit dispersion phenomena. Specifically, their conductivity increases with frequency while their permittivity decreases with frequency [10]–[12]. This dispersive behavior is classified into different regimes based on the mechanisms involved in the tissue-field interactions [13]. The region of the dielectric spectrum is of interest in EIT is the β dispersion which covers radio frequencies ($1\ \text{kHz} < f < 100\ \text{MHz}$) and is primarily associated with the capacitive nature of cell membranes and the rotational relaxation of biomacromolecules. Therefore, tissue characterization becomes possible in terms of dispersion parameters if multifrequency measurements are obtained. Since the characteristic impedance for breast tissue lies above 1 MHz and our previous clinical studies have suggested that better detection occurs with higher frequencies, it was natural to extend the excitation frequency range of our imaging system. A significant effort is required to design and develop high frequency (HF) EIT systems. Dartmouth's most recent DSP-based instrumentation possesses 64 channels that can operate up to 10 MHz with a signal-to-noise ratio better than 95 dB [14]. Since HF data is acquired, it is important to explore a HF numerical model to ensure accurate image reconstruction.

In this paper, the complete wave equation for HF EIT is solved through scalar and vector potentials. The advantage of this formulation is that it provides a convenient way of imposing boundary conditions on the electrodes in terms of

Manuscript received January 10, 2005; revised October 4, 2005. This work was supported in part by the National Institutes of Health (NIH) National Cancer Institute under Grant P01-CA80139. The Associate Editor responsible for coordinating the review of this paper an recommending its publication was C. McLeod. *Asterisk indicates corresponding author.*

*N. K. Soni is with the Philips Medical Systems, Cleveland, OH 44143 USA (e-mail: nksoni@yahoo.com).

K. D. Paulsen, H. Dehghani, and A. Hartov are with the Thayer School of Engineering, Dartmouth College, Hanover, NH 03755 USA

Digital Object Identifier 10.1109/TMI.2005.861001

the data supplied by an EIT system. Standard finite element methods (FEMs) can still be used for the numerical computation without extending the domain by incorporating impedance boundary conditions (IBCs) over portions of the surface not covered by electrodes. A complete inversion algorithm is realized that effectively constructs the Jacobian required for electrical property updating through adjoint field computations. In the following sections, we summarize this FEM formulation, which has adapted the numerical development in [19] and [20] to the EIT inversion problem. Simulation and experimental results are presented which demonstrate that the algorithm has been successfully implemented, performs equivalently to its Laplace counterpart for frequencies below 1 MHz, but out-performs the Laplace model when the signal frequency reaches 10 MHz. Importantly, these numerical findings are consistent with theoretical expectations, making the software approach particularly attractively because it returns the proper physical behavior for both high and low frequency signals without alteration.

II. Problem Formulation

Source-free Maxwell's equations for sinusoidal excitation $(e^{-j\omega t})$ can be expressed as

$$\boldsymbol{\nabla}\times\mathbf{E}=j\omega\mu\mathbf{H} \tag{1}$$

$$\boldsymbol{\nabla}\times\mathbf{H}=-j\omega\epsilon^{*}\mathbf{E} \tag{2}$$

$$\boldsymbol{\nabla}\cdot\epsilon^{*}\mathbf{E}=0 \tag{3}$$

$$\boldsymbol{\nabla}\cdot\mu\mathbf{H}=0 \tag{4}$$

where $\mathbf{E}$ is the electrical field phasor, $\mathbf{H}$ is the magnetic field phasor, ω is the excitation frequency, μ is the permeability, and ϵ^{*} is the complex permittivity of the medium. The double curl and divergence equations in terms of the electric field can be derived from (1)–(4) by eliminating $\mathbf{H}$

$$\boldsymbol{\nabla}\times\left(\frac{1}{j\omega\mu}\boldsymbol{\nabla}\times\mathbf{E}\right)+j\omega\epsilon^{*}\mathbf{E}=0 \tag{5}$$

$$\boldsymbol{\nabla}\cdot\epsilon^{*}\mathbf{E}=0. \tag{6}$$

The above equations can be re-expressed in terms of potentials using the definition of $\mathbf{E}$

$$\mathbf{E}=-\boldsymbol{\nabla}\Phi+j\omega\mathbf{A} \tag{7}$$

where Φ is the scalar electric potential and $\mathbf{A}$ is the vector magnetic potential. According to Helmholtz's theorem a vector field is completely determined if both its divergence and curl are specified. Since the curl of $\mathbf{A}$ is exactly equal to the magnetic flux density $\mathbf{B}$, where $\mathbf{B}=\boldsymbol{\nabla}\times\mathbf{A}$, the divergence of $\mathbf{A}$ is also needed for a unique solution of the potentials. Different choices of divergence of $\mathbf{A}$ are known as gauge conditions [15]. The Lorentz gauge is a common choice for wave propagation problems and can be constructed to have desirable mathematical and numerical properties. Specially, selecting

$$\boldsymbol{\nabla}\cdot\mathbf{A}=j\omega\mu\epsilon^{*}\Phi \tag{8}$$

generates continuous potentials in electrically heterogeneous media that obey the coupled set of partial differential equations

$$\boldsymbol{\nabla}\times\left(\frac{1}{\mu}\boldsymbol{\nabla}\times\mathbf{A}\right)-\boldsymbol{\nabla}\left(\frac{1}{\mu}\boldsymbol{\nabla}\cdot\mathbf{A}\right)-\omega^{2}\epsilon^{*}\mathbf{A}+j\omega\Phi\boldsymbol{\nabla}\epsilon^{*}=0 \tag{9}$$

$$\boldsymbol{\nabla}\cdot\epsilon^{*}\boldsymbol{\nabla}\Phi+\omega^{2}\epsilon^{*2}\mu\Phi-j\omega\mathbf{A}\cdot\boldsymbol{\nabla}\epsilon^{*}=0. \tag{10}$$

This formulation has previously been shown to eliminate nonphysical numerical solutions that are produced when nodal-based FEM techniques are applied to the double curl operator [16]–[20]. FEM implementation of (9) and (10) eliminate these nonphysical solutions by introducing well-behaved Helmholtz-like operators written in terms of potentials. Thus, the governing equations are expressed in $\mathbf{A}$ and Φ and involve four degrees of freedom per node (A_x, A_y, A_z, and Φ) in three dimensions. This additional cost is offset by the removal of nonphysical numerical artifacts from the computations and the advantages of having boundary conditions arise in terms of the physical quantities supplied by the EIT hardware. A weak formulation can be derived by the Galerkin weighted residual method for a nodal FEM solution by weighting (9) and (10) with nodal scalar basis functions ϕ_i and integrating

$$\begin{aligned}&\left\langle\left(\frac{1}{\mu}\boldsymbol{\nabla}\times\mathbf{A}\right)\times\boldsymbol{\nabla}\phi_i\right\rangle+\left\langle\left(\frac{1}{\mu}\boldsymbol{\nabla}\cdot\mathbf{A}\right)\boldsymbol{\nabla}\phi_i\right\rangle\\&\quad-\langle\omega^{2}\epsilon^{*}\mathbf{A}\phi_i\rangle-\langle j\omega\epsilon^{*}\boldsymbol{\nabla}(\Phi\phi_i)\rangle\\&\quad=-\oint\hat{\mathbf{n}}\times\left(\frac{1}{\mu}\boldsymbol{\nabla}\times\mathbf{A}\right)\phi_i ds\\&\qquad+\oint\hat{\mathbf{n}}\left(\frac{1}{\mu}\boldsymbol{\nabla}\cdot\mathbf{A}-j\omega\epsilon^{*}\Phi\right)\phi_i ds\end{aligned} \tag{11}$$

$$\begin{aligned}&\langle\boldsymbol{\nabla}\phi_i\cdot\epsilon^{*}\boldsymbol{\nabla}\Phi\rangle-\langle\omega^{2}\epsilon^{*2}\mu\Phi\phi_i\rangle-\langle j\omega\epsilon^{*}\boldsymbol{\nabla}\cdot(\phi_i\mathbf{A})\rangle\\&\quad=-\oint\hat{\mathbf{n}}\cdot\epsilon^{*}(j\omega\mathbf{A}-\boldsymbol{\nabla}\Phi)\phi_i ds\end{aligned} \tag{12}$$

where $\langle\cdot\rangle$ represents domain integration and ϕ_i are the local basis functions for a given mesh. The expansion of $\mathbf{A}$ and Φ in terms of basis functions ϕ_j results in a symmetric system of algebraic equations

$$\Sigma_j\mathbf{K}_{ij}F_j=R_i \tag{13}$$

(See (14) and (15) at the bottom of the page.) For simplificity, we present and implement the two-dimensional case (F_j =

$$\mathbf{K}_{ij}=\begin{bmatrix}\left\langle\frac{1}{\mu}\boldsymbol{\nabla}\phi_j\cdot\boldsymbol{\nabla}\phi_i\right\rangle-\langle\omega^{2}\epsilon^{*}\phi_i\phi_j\rangle & \left\langle\frac{1}{\mu}\left(-\frac{\partial\phi_j}{\partial y}\frac{\partial\phi_i}{\partial y}+\frac{\partial\phi_j}{\partial y}\frac{\partial\phi_i}{\partial x}\right)\right\rangle & \left\langle-j\omega\epsilon^{*}\left(\phi_i\frac{\partial\phi_j}{\partial x}+\phi_j\frac{\partial\phi_i}{\partial x}\right)\right\rangle\\ \left\langle\frac{1}{\mu}\left(-\frac{\partial\phi_j}{\partial y}\frac{\partial\phi_i}{\partial x}+\frac{\partial\phi_j}{\partial x}\frac{\partial\phi_i}{\partial y}\right)\right\rangle & \left\langle\frac{1}{\mu}\boldsymbol{\nabla}\phi_j\cdot\boldsymbol{\nabla}\phi_i\right\rangle-\langle\omega^{2}\epsilon^{*}\phi_i\phi_j\rangle & \left\langle-j\omega\epsilon^{*}\left(\phi_i\frac{\partial\phi_j}{\partial y}+\phi_j\frac{\partial\phi_i}{\partial y}\right)\right\rangle\\ \left\langle-j\omega\epsilon^{*}\left(\phi_j\frac{\partial\phi_i}{\partial x}+\phi_i\frac{\partial\phi_j}{\partial x}\right)\right\rangle & \left\langle-j\omega\epsilon^{*}\left(\phi_j\frac{\partial\phi_i}{\partial y}+\phi_i\frac{\partial\phi_j}{\partial y}\right)\right\rangle & \langle\epsilon^{*}\boldsymbol{\nabla}\phi_j\cdot\boldsymbol{\nabla}\phi_i\rangle-\langle\omega^{2}\epsilon^{*2}\mu\phi_i\phi_j\rangle\end{bmatrix} \tag{14}$$

$$R_i=\begin{Bmatrix}\hat{\mathbf{x}}\cdot\left(-\oint\hat{\mathbf{n}}\times\left(\frac{1}{\mu}\boldsymbol{\nabla}\times\mathbf{A}\right)\phi_i ds\right)+\oint\hat{\mathbf{n}}\left(\frac{1}{\mu}\boldsymbol{\nabla}\cdot\mathbf{A}-j\omega\epsilon^{*}\Phi\right)\phi_i ds\\ \hat{\mathbf{y}}\cdot\left(-\oint\hat{\mathbf{n}}\times\left(\frac{1}{\mu}\boldsymbol{\nabla}\times\mathbf{A}\right)\phi_i ds\right)+\oint\hat{\mathbf{n}}\left(\frac{1}{\mu}\boldsymbol{\nabla}\cdot\mathbf{A}-j\omega\epsilon^{*}\Phi\right)\phi_i ds\\ -\oint\hat{\mathbf{n}}\cdot\epsilon^{*}(j\omega\mathbf{A}-\boldsymbol{\nabla}\Phi)\phi_i ds\end{Bmatrix} \tag{15}$$

$\{A_{xj}, A_{yj}, \Phi\}$) where the system matrix and right-hand side forcing vector are given by (14) and (15), respectively [21].

The traditional numerical model (Laplace's equation) for low frequencies can be reached directly from (2) by taking divergence on both sides of the equation and assuming $\mathbf{E}$ in (7) is representable only by $\nabla\Phi$ in which case the Galerkin weighted residual method for nodal FEM is

$$\nabla \cdot \sigma^* \nabla \Phi = 0 \tag{16}$$

$$\langle \sigma^* \nabla \Phi \cdot \nabla \phi_i \rangle = \oint \hat{\mathbf{n}} \cdot \sigma^* \nabla \Phi \phi_i ds \tag{17}$$

where σ^* is the complex conductivity.

III. Boundary Conditions

The FEM formulation of the physical problem results in the system of equations expressed in global x, y coordinates (13) whereas the boundary conditions for vector potentials are prescribed in a local coordinate system of normal and tangential components. Therefore, the system of equations is transformed to local coordinates through a rotation matrix during the assembly process

$$[\mathbf{R}_i] = \begin{bmatrix} \cos\theta_i & \sin\theta_i & 0 \\ -\sin\theta_i & \cos\theta_i & 0 \\ 0 & 0 & 1 \end{bmatrix} \tag{18}$$

where θ_i is dictated by the nodal normal. Once the solution is obtained it can be transferred back to global x, y coordinates by $[\mathbf{R}_i]^{-1}$.

The advantage of (11) and (12) is that the boundary integral terms can be used to implement certain constraints. Boundary conditions for the model, (13), depend on the excitation mode. Two types of excitations are most often used in EIT, the voltage mode and the current mode. In the voltage mode, voltages are applied and currents are measured while in the current mode, currents are applied and voltages are measured. In this presentation, we develop the voltage mode explicitly where we also consider two different conditions for the intervening surfaces between electrodes as outlined below.

A. Mixed Boundary Conditions

For the voltage mode, mixed boundary conditions can be applied such that the following hold.

- *On the electrodes:* $\Phi = V_{\text{applied}}$ for the scalar potential and $A_t = 0$ for the tangential component of the vector potential. Here, a homogeneous Neumann condition is specified in the normal projection of (11) by enforcing the gauge condition in its boundary integral.
- *Between the electrodes:* $\partial\Phi/\partial n = 0$ and $A_n = 0$ leading to a homogeneous Neumann condition for the scalar potential (12) and a Dirichlet condition ($A_n = 0$) instead of the normal projection of the vector potential (11). In this case, the tangential projection of (11) is retained and calls for the boundary integral of tangential $\mathbf{H}$ which is assumed to be zero.

Operationally, the type I conditions on the electrodes are introduced into the system in (13) by removing the Galerkin equations on electrode nodes associated with (12) for the scalar potential and the tangential projection of (11) for the vector potential in favor of the known information. Similar maneuvers occur at nodes between electrodes in the case of the normal projection of (11). The remaining right-hand-sides both on and off the electrodes are zero because of the respective homogeneous Neumann conditions applied in the corresponding boundary integrals. These conditions are easy to implement but since they prevent the fields from radiating into the exterior domain in between the electrodes, they result in a Laplace-like solution.

B. Impedance Boundary Conditions

As an improvement, an approximation can be invoked between the electrodes to represent the propagating characteristics of the field. In theory, the field is unbounded and, therefore, free to radiate into the surrounding space from the domain's external surface, technically requiring an extension of the computational mesh beyond the imaging field of view. In practice, the mesh can be truncated and an approximate radiation or IBC can be applied which relates the components of $\mathbf{A}$ and Φ in order to generate a closed numerical model leading to a unique solution [22]. Thus, in the boundary integrals of (11) and (12) instead of homogeneous Neumann conditions (on tangential component of $\mathbf{H}$ and normal component of $\mathbf{J}$) as in the nonradiating, quasi-static limit, the IBC allows a normal current density and tangential component of $\nabla \times \mathbf{A}$ to develop in the solution at these locations (i.e., in between the finite-sized electrodes).

The IBC is implemented by evaluating the boundary integrals in (11) and (12) and adding this contribution to the system matrix for the boundary segments in between the electrodes. For (11) the tangential projection is equivalent to the surface current ($\mathbf{J}_s$) which is proportional to the tangential electric field ($\mathbf{E}_s$)

$$\oint \hat{\mathbf{n}} \times \left(\frac{1}{\mu} \nabla \times \mathbf{A} \right) ds = \oint \mathbf{J}_s ds = \frac{1}{Z_s} \oint \nabla_s \cdot (-\nabla_s \Phi + j\omega \mathbf{A}_s) ds \tag{19}$$

where Z_s is the surface impedance

$$Z_s = \sqrt{\frac{\mu}{\epsilon}} = \frac{Z_0}{\sqrt{\epsilon_r}}. \tag{20}$$

Here, Z_0 is the characteristic impedance of free space (377 Ω), ϵ_r is the relative permittivity of the medium, $\mathbf{A}_s$ is the tangential projection of $\mathbf{A}$ ($\mathbf{A}_s = \hat{\mathbf{n}} \times \mathbf{A}$), and ∇_s is the surface divergence expressed in cartesian coordinates

$$\nabla_s = \frac{\Delta x}{\Delta s} \frac{\partial}{\partial x} \hat{\mathbf{i}} + \frac{\Delta y}{\Delta s} \frac{\partial}{\partial y} \hat{\mathbf{j}} \tag{21}$$

along an element on the boundary where Δs is the element length while Δx and Δy are the signed differences in the x and y coordinates of the two nodes comprising the boundary element.

Similarly, for (12) the normal projection of electric field can be evaluated using

$$\oint \hat{\mathbf{n}} \cdot \epsilon (j\omega \mathbf{A} - \nabla \Phi) ds = \oint \frac{1}{j\omega} \nabla_s \cdot \mathbf{J}_s = \frac{1}{j\omega Z_s} \oint \nabla_s \cdot (-\nabla_s \Phi + j\omega \mathbf{A}) ds. \tag{22}$$

The IBC noted here should not be confused with the complete electrode model generally used in the EIT literature which incorporates the effect of electrode polarization due to chemical

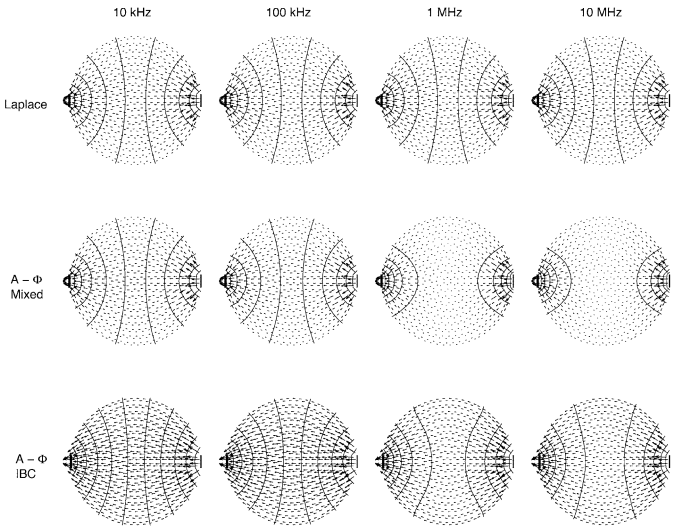

Fig. 1. Voltage and electric field distributions for Laplace and $(\mathbf{A}, \Phi)$ solutions for a circular domain with material properties $\sigma = 2\ \mathrm{Sm}^{-1}$, $\epsilon_r = 80$. Two electrodes (right at $+1$ V and left at -1 V) were used for excitation over the frequency range 10 kHz to 10 MHz. The surface impedance factor was 0.024 S for the $(\mathbf{A}, \Phi)$ solution with IBCs.

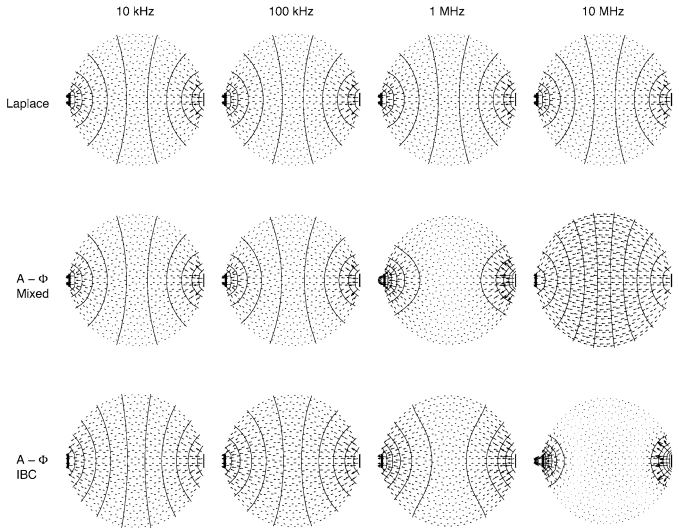

Fig. 2. Voltage and electric field distributions for the Laplace and $(\mathbf{A}, \Phi)$ solutions on a circular domain with material properties $\sigma = 2\ \mathrm{Sm}^{-1}$, $\epsilon_r = 8000$. Two electrodes (right at $+1$ V and left at -1 V) were used for excitation over the frequency range 10 kHz to 10 MHz. The surface impedance factor was same as in Fig. 1.

effects at the object-electrode interface [25]. In this paper, the shunt electrode model has been used in the Φ solution for simplicity but the complete electrode model is readily implemented through the boundary integrals in (11) and (12) by introducing a separate impedance relationship on the electrodes.

IV. Model Calculations

An attractive feature of this $(\mathbf{A}, \Phi)$ formulation is that as the signal frequency is reduced, the field model and the associated reconstruction algorithm collapse to the quasi-static limit and, therefore, mimic the behavior of the Laplace model. This provides a means of performing checks on the HF $(\mathbf{A}, \Phi)$ algorithm at the lower frequencies where the Laplace's algorithm is valid. Further, synthetic data generated at high frequencies can be used to evaluate the performance of the Laplace model for image reconstruction. However, care must be exercised when computing the boundary currents since for the Laplace model they are dictated by the complex conductivity (σ^*) while for the $(\mathbf{A}, \Phi)$ formulation they are modulated by the complex permittivity (ϵ^*). In order to compare the two boundary currents, the relationship $\sigma^* = -j\omega\epsilon^*$ must be used. In the voltage mode, the discarded Galerkin equations from (12) are summed over each electrode and the resulting $(\mathbf{A}, \Phi)$ solution is used to compute its left-hand-side which defines the boundary integral in (12) that is exactly the model estimate of the driving current for image reconstruction.

To illustrate certain characteristics of the field behavior, consider a system of two electrodes each of length 12 mm with $+1$ and -1 volt excitation over a range of frequencies (10 kHz to 10 MHz) applied to a circular domain of 10 cm in diameter with material properties $\sigma = 2\ \mathrm{Sm}^{-1}$, $\epsilon_r = 80$ and $\mu_r = 1.0$. Fig. 1 depicts the resulting isopotential contours and electric field using the Laplace and $(\mathbf{A}, \Phi)$ formulations. The electric field was evaluated at element centroids using (7). The Laplace model predicts scalar field and potential distributions which do not vary with frequency, whereas the $(\mathbf{A}, \Phi)$ formulation exhibits the expected frequency dependence of the fields. As the excitation frequency increases, the field becomes more superficial and confined toward the periphery near the electrodes. This is better demonstrated with the $(\mathbf{A}, \Phi)$ formulation using an IBC with a surface impedance factor $1/Z_s = \sqrt{80}/377 = 0.024$ S. Since the mixed boundary conditions for the $(\mathbf{A}, \Phi)$ formulation do not allow the field to radiate between the electrodes it becomes more concentrated near them.

The behavior of electromagnetic waves in a medium is influenced by its characteristic impedance and the excitation frequency. An example of impedance mismatch is illustrated in Fig. 2. Here, the material's relative permittivity is increased to 8000, which implies a significant reduction in its characteristic impedance. However, the same surface impedance factor $(1/Z_s = 0.024\ \mathrm{S})$ was used in the calculations. Again, the Laplace model describes the same field behavior across frequencies while the $(\mathbf{A}, \Phi)$ formulation reflects the field behavior associated with the impedance mismatch. With mixed boundary conditions the $(\mathbf{A}, \Phi)$ field magnitude is reduced within the medium at higher frequencies whereas with the IBC it is confined near the electrodes. It should be noted here that only the real part of the field is plotted in Figs. 1 and 2. As the frequency increases the imaginary component comes into play which contributes toward the total magnitude of the field.

The same behavior is less apparent in a 16 electrode configuration with trigonometric excitation at the lowest spatial frequency. Here, the boundary currents can be used to analyze the model behavior (Fig. 3). Since the $(\mathbf{A}, \Phi)$ formulation with mixed boundary conditions is biased toward the Laplace solution, the two boundary currents are almost identical whereas the boundary currents in the $(\mathbf{A}, \Phi)$ formulation with an IBC are dependent on the characteristic impedance of the medium and their magnitude is somewhat lower than the others because some of the current density is allowed to escape between the electrodes by radiating outside the medium.

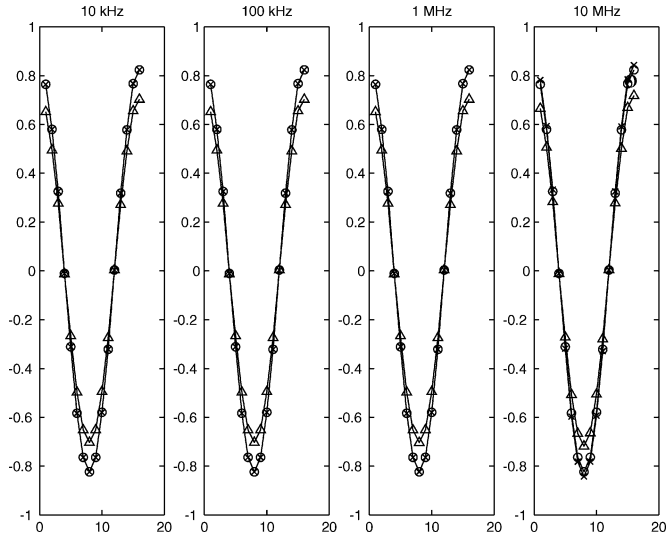

Fig. 3. Boundary currents for Laplace ($\circ$), ($\mathbf{A}$, Φ) mixed (x), and ($\mathbf{A}$, Φ) IBC (Δ) solutions for a circular domain with material properties $\sigma = 2\ \mathrm{Sm}^{-1}$ and $\epsilon_r = 80$. Sixteen electrodes were used with trigonometric excitation of the first spatial pattern over the frequency range 10 kHz–10 MHz. The surface impedance factor was 0.024 S for ($\mathbf{A}$, Φ) solution with IBC condition.

V. Image Reconstruction

In the EIT reconstruction problem, the objective is to recover material properties (σ, ϵ_r) at mesh nodes using boundary electrical measurements. We exploit a least-squares approach to minimize the difference between measured and calculated data using the following objective function for boundary current minimization during operation in the voltage mode

$$\psi = \|I_{\mathrm{meas}} - I_{\mathrm{cal}}\|^2 + \lambda \|L\sigma^*\|^2 \tag{23}$$

where I_{meas} is the measured current density, I_{cal} is the model calculated current density, λ is regularization parameter and L is regularization matrix. The regularization parameter penalizes the solution so that highly oscillatory behavior is damped. The regularization matrix L is generated to mirror a finite difference approximation for the first derivative such that [23]

$$\begin{aligned} L(i,j) &= -1, \quad \text{for } i \neq j \\ L(i,j) &= \left|\Sigma_j L(i,j)\right|, \quad \text{for } i = j \end{aligned} \tag{24}$$

While we did not make any explicit comparison with the simple identity matrix as the regularization in this paper, our accumulated experience has shown that (24) is better suited to discrete inclusion detection because it reduces property variation in the estimates without over-smoothing the jump change in properties that occurs at the inclusion boundary. The regularization parameter λ was selected empirically as 1e-4.

The objective function for minimization is differentiated with respect to the material properties and the resulting system of nonlinear equations is solved using Newton's method where the complex conductivity update is given by

$$\delta\sigma^* = \left(J^T J + \lambda L^T L\right)^{-1} \left\{J^T (I_{\mathrm{meas}} - I_{\mathrm{cal}}) - \lambda L^T L \sigma^*\right\} \tag{25}$$

Here, J is the sensitivity matrix or Jacobian that represents the rate of change of measurements with respect to material property variations. The Jacobian was computed using the adjoint method [24]. For the ($\mathbf{A}$, Φ) formulation, we compute the following expression for the Jacobian construction [8]:

$$J = \left\langle \mathbf{E}_{\mathrm{direct}}, \mathbf{E}^*_{\mathrm{adjoint}} \right\rangle \tag{26}$$

where $\mathbf{E}_{\mathrm{direct}}$ is the nodal electric field for applied patterns and $\mathbf{E}^*_{\mathrm{adjoint}}$ is the complex conjugate nodal electric field using adjoint sources. In either case, the electric field is calculated at mesh nodes in a postprocessing step using (7) and the Galerkin weighted residuals method

$$\sum_j \langle \phi_i, \phi_j \rangle \mathbf{E}_j = \langle (-\boldsymbol{\nabla}\Phi + j\omega\mathbf{A}), \phi_i \rangle \tag{27}$$

once the potentials are known through solution of (13) at the current property distribution estimate.

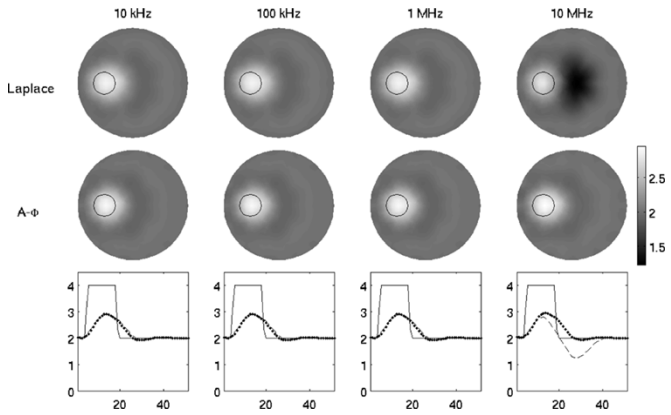

Fig. 4. Reconstruction results for noise-free data. Laplace reconstructions are illustrated in the top row, ($\mathbf{A}$, Φ) reconstructions in the middle row, while the bottom row compares the cross sections of simulated and reconstructed conductivity profiles. The circle in the first two rows represents the location of a simulated inclusion. For the conductivity cross section, the solid line represents the simulated conductivity, dotted line the ($\mathbf{A}$, Φ), and dashed line, the Laplace results.

VI. Simulation Results

Numerical simulations for image reconstructions were performed on a circular domain of 10 cm in diameter with material properties $\sigma = 2\ \mathrm{Sm}^{-1}$, $\epsilon_r = 80$, and $\mu_r = 1$. A higher conductivity inclusion of 2 cm in diameter about 2 cm from the mesh external edge with $\sigma = 4\ \mathrm{Sm}^{-1}$ was also included in the domain. The data generation mesh (1463 nodes and 2793 elements) was different from the field mesh (1345 nodes and 2600 elements) and the property mesh (353 nodes and 1400 elements) in the reconstructions. Noise-free data were generated at four frequencies of 10 kHz, 100 kHz, 1 MHz, and 10 MHz covering the present excitation range of our EIT system using the $(\mathbf{A}, \Phi)$ formulation with mixed boundary conditions.

Fig. (4) illustrates the reconstruction results from the Laplace and ($\mathbf{A}$, Φ) models. Five iterations were performed in either case starting with background property values as the initial estimate ($\sigma = 2\,\mathrm{Sm}^{-1}, \epsilon_r = 80$). The top row corresponds to the Laplace reconstructions, the middle row corresponds to ($\mathbf{A}$, Φ) reconstructions. A comparison of reconstructed cross-sectional profiles across the domain with the original simulation geometry is depicted in the third row. It can be observed from the images that for low frequencies (up to 1 MHz) the two models seem to recover almost the same conductivity values. However, at 10 MHz the Laplace model breaks down and a region of low conductivity

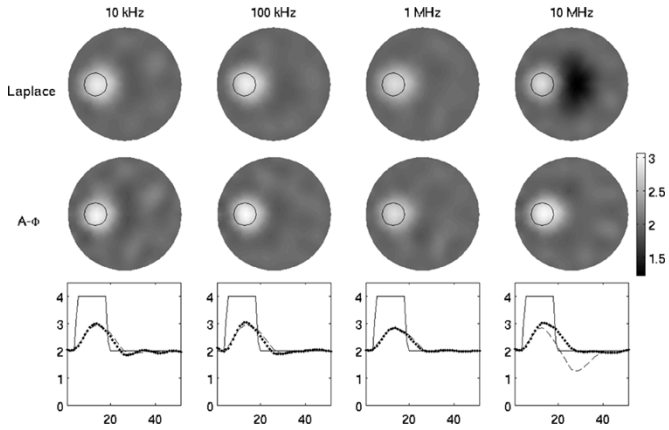

Fig. 5. Effect of 1% noise on reconstructions. Laplace reconstructions are illustrated in the top row, ($\mathbf{A}$, Φ) reconstructions in the middle row, while the bottom row compares the cross sections of simulated and reconstructed conductivity profiles. The circle in the first two rows represents the location of a simulated inclusion. For the conductivity cross section, the solid line represents the simulated conductivity, dotted line the ($\mathbf{A}$, Φ) and dashed line the Laplace results.

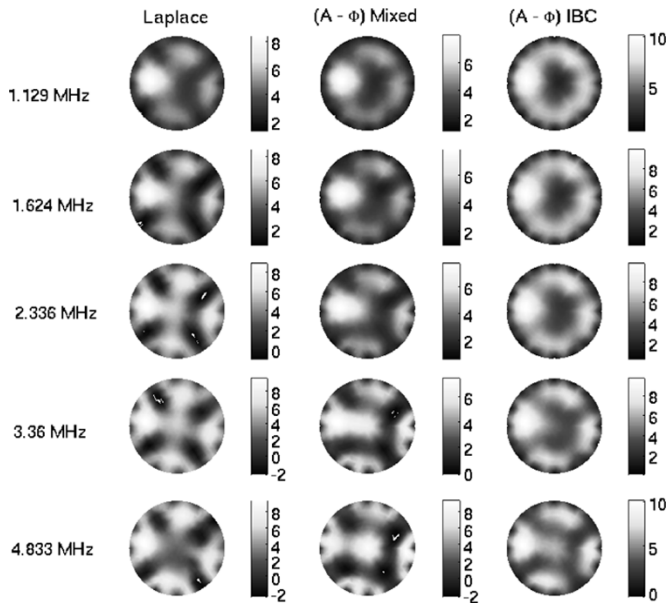

Fig. 6. Comparing reconstruction results for the data acquired on a saline tank with brass conductor as an inclusion. Notice at 1.1 MHz the three reconstruction algorithms perform almost similar but characteristic patterns appear at higher frequencies. ($\mathbf{A}$, Φ) formulation with IBC seems to recover conductor better than Laplace or ($\mathbf{A}$, Φ) with mixed boundary conditions.

emerges in the center of the image. The ($\mathbf{A}$, Φ) reconstruction still recovers the inclusion without excessive artifacts.

The effect of noise is illustrated in Fig. 5 where 1% was added to the data. Although this amount represents a significant noise level for an EIT system, the ($\mathbf{A}$, Φ) reconstruction algorithm continues to work well. The noise effect causes a degradation in the reconstructed images which is highest at 10 MHz using the Laplace model. The reconstructed images are less affected by noise for the entire range of the excitation frequencies using the ($\mathbf{A}$, Φ) algorithm even at 10 MHz where the original location of the inclusion and the background values are preserved.

VII. Experimental Results

Fig. 6 compares reconstruction results using both Laplace and ($\mathbf{A}$, Φ) formulations for the data acquired on a cylindrical tank filled with 0.9% saline using Dartmouth's HF system. The tank was 8.5 cm in diameter and was filled about 1.2 cm in height. A brass conductor of diameter 1.5 cm was used as an inclusion which was located at 9 o'clock in the tank. Reconstructed images are presented here for the frequency range from 1.1 MHz to 4.8 MHz because the results are identical from the two numerical models for lower frequencies. For ($\mathbf{A}$, Φ) formulation with IBC, an impedance factor equal to the characteristic impedance of the medium was used in the calculations $(1/Z_s = \sqrt{80}/377 = 0.024\,\mathrm{S})$. The conductor is well localized over the entire frequency range using ($\mathbf{A}$, Φ) formulation with IBC with minimum edge artifacts while the Laplace reconstruction suffers from considerable artifacts and the ($\mathbf{A}$, Φ) formulation with mixed boundary conditions falls in between the two. Although preliminary and certainly far from conclusive, these results suggest that the ($\mathbf{A}$, Φ) formulation with IBC is better suited for reconstructing the HF data.

VIII. Discussion

With the development of more advanced EIT systems [14] it is now possible to explore new medical opportunities with HF imaging, 3-D imaging and dynamic imaging. Generally, low frequency excitation has been used in EIT which results in a numerical model governed by Laplace's equation. Since at higher frequencies both the electric and the magnetic fields are coupled yet the EIT excitation occurs in terms of voltages (and/or currents), the need arises for a better numerical model. This paper illustrates the implementation of a HF model consisting of a scalar/vector potential formulation ($\mathbf{A}$, Φ), and the corresponding inversion scheme to recover material properties for EIT using FEM. The field behavior in simulation results shows that at higher frequencies the Laplace model does not adequately represent the wave phenomena whereas the ($\mathbf{A}$, Φ) formulation is valid for the full frequency range including low frequencies where it mimics the Laplace solution. These trends were also evident in images reconstructed from both simulated and experimental data over a range of frequencies of interest in EIT.

References

[1] M. Cheney, D. Isaacson, and J. C. Newell, "Electrical Impedance Tomography," *SIAM Rev.*, vol. 41, pp. 85–101, 1999.

[2] D. C. Barber and B. H. Brown, "Applied potential tomography," *J. Phys. E. Sci. Instrum.*, vol. 17, pp. 723–733, 1984.

[3] B. H. Brown, "Medical impedance tomography and process impedance tomography: a brief review," *Meas. Sci. Technol.*, vol. 12, pp. 991–996, 2001.

[4] W. R. B. Lionheart, "EIT reconstruction algorithms: pitfalls, challenges and recent developments," *Physiol. Meas.*, vol. 25, pp. 125–142, 2004.

[5] A. Hartov, T. E. Kerner, and K. D. Paulsen, "Simulation of error propagation in finite element image reconstruction for electrical impedance tomography," *Meas. Sci. Technol.*, vol. 12, pp. 1040–1049, 2001.

[6] A. Hartov, E. Demidenko, N. Soni, M. Markova, and K. D. Paulsen, "Using voltage sources as current drivers for electrical impedance tomography," *Meas. Sci. Technol.*, vol. 13, pp. 1425–1430, 2002.

[7] T. E. Kerner, A. Hartov, K. S. Osterman, C. DeLorenzo, and K. D. Paulsen, "An improved data acquisition method for electrical impedance tomography," *Physiol. Meas.*, vol. 22, pp. 31–38, 2001.

[8] E. Somersalo, D. Isaacson, and M. Cheney, "A linearized inverse boundary value problem for Maxwell's equations," *J. Comput. Appl. Math.*, vol. 42, pp. 123–136, 1992.

[9] B. H. Doerstling, "A 3-D reconstruction algorithm for the linearized inverse boundary value problem for Maxwell's equations," PhD Thesis, Rensselaer Polytechnique Institute, Troy, NY, 1995.

[10] R. Petigh, "Dielectric properties of body tissues," *Clin. Phys. Physiol. Meas.*, vol. 8, no. Suppl. A, pp. 5–12, 1987.

[11] J. Jossinet, "The impedivity of freshly excised human breast tissue," *Physiol. Meas.*, vol. 19, pp. 61–75, 1998.

[12] E. T. McAdams and J. Jossinet, "Tissue impedance: a historical overview," *Physiol. Meas.*, vol. 16, pp. A1–A13, 1995.

[13] Ø G. Martinsen, S. Grimmes, and H. P. Schwan, "Interface phenomena and dielectric properties of biological tissue," in *Encylopedia of Surface and Colloidal Science*. New York: Marcel Dekker, 2002, pp. 2643–2652.

[14] R. Halter, A. Hartov, and K. D. Paulsen, "Design and implementation of a high frequency electrical impedance tomography system," *Physiol. Meas.*, vol. 25, pp. 379–390, 2004.

[15] P. P. Silvester and R. L. Ferrari, *Finite Elements for Electrical Engineers*. New York: Cambridge Univ. Press, 1996.

[16] D. R. Lynch and K. D. Paulsen, "Origin of vector parasites in numerical Maxwell solutions," *IEEE Trans. Microw. Theory Tech.*, vol. 39, no. 3, pp. 389–394, Mar. 1991.

[17] D. R. Lynch, K. D. Paulsen, and W. E. Boyse, "Synthesis of vector parasites in finite element Maxwell solutions," *IEEE Trans. Microw. Theory Tech.*, vol. 41, no. 8, pp. 1439–1448, Aug. 1991.

[18] K. D. Paulsen and D. R. Lynch, "Elimination of vector parasites in finite element Maxwell solutions," *IEEE Trans. Microw. Theory Tech.*, vol. 39, no. 3, pp. 395–404, Mar. 1991.

[19] K. D. Paulsen, W. E. Boyse, and D. R. Lynch, "Continuous potential Maxwell solutions on nodal-based finite elements," *IEEE Trans. Antennas Propag.*, vol. 40, no. 10, pp. 1192–1200, Oct. 1992.

[20] W. E. Boyse, D. R. Lynch, and G. N. Minerbo, "Nodal-based finite element modeling of Maxwell's equations," *IEEE Trans. Antennas Propag.*, vol. 40, no. 6, pp. 642–651, Jun. 1992.

[21] D. R. Lynch, *Numerical Partial Differential Equations for Environmental Scientists and Engineers—A First Practical Course*. New York: Springer, 2004.

[22] W. E. Boyse and K. D. Paulsen, "Accurate solution of Maxwell's equations around PEC corners and highly curved surfaces using nodal finite elements," *IEEE Trans. Antennas Propag.*, vol. 45, no. 12, pp. 1758–1767, Dec. 1997.

[23] B. Brandstätter, K. Hollaus, H. Hutten, M. Mayer, R. Merwa, and H. Scharfetter, "Direct estimation of Cole parameters in multifrequency EIT using a regularized Gauss-Newton method," *Physiol. Meas.*, vol. 24, pp. 437–448, 2003.

[24] N. Polydorides and W. R. B. Lionheart, "A Matlab toolkit for three-dimensional electrical impedance tomography: a contribution to the electrical impedance and diffuse optical reconstruction software project," *Meas. Sci. Technol.*, vol. 13, pp. 1871–1883, 2002.

[25] E. Somersalo, M. Cheney, and D. Isaacson, "Existence and uniqueness for electrode models for electrical current computed tomography," *SIAM J. Appl. Math.*, vol. 52, pp. 1023–1040, 1992.